Soft Matter

PAPER

View Article Online
View Journal | View Issue

Cite this: *Soft Matter*, 2021, **17**, 2985

Active motion of multiphase oil droplets: emergent dynamics of squirmers with evolving internal structure†

Xin Wang, ‡[a] Rui Zhang,‡§[b] Ali Mozaffari,[b] Juan J. de Pablo *[bc] and Nicholas L. Abbott *[a]

Received 20th October 2020,
Accepted 15th January 2021

DOI: 10.1039/d0sm01873b

rsc.li/soft-matter-journal

Synthetic soft matter systems, when driven beyond equilibrium by active processes, offer the potential to achieve dynamical states and functions of a complexity found in living matter. Emulsions offer the basis of a simple yet versatile system for identification of the physicochemical principles underlying active soft matter, but how multiple internal phases within emulsion droplets (*e.g.*, Janus morphologies) organize to impact emergent dynamics is not understood. Here, we create multiphase oil droplets with ultralow interfacial tensions but distinct viscosities, and drive them into motion in aqueous micellar solutions. Preferential solubilization of select components of the oil both drives the droplet motion and yields a progression of internal phase morphological states with distinct symmetries. We find the active droplets to exhibit five dynamical states during morphogenesis. By quantifying microscopic flow fields, we show that it is possible to map the diverse droplet behaviors to squirmer models of spherical microswimmers in Stokes flow, thus showing that multiphase droplets offer the basis of a versatile platform with which to study and engineer the hydrodynamics of microswimmers.

Introduction

Recent studies of active soft matter,[1–5] including self-propelled colloids (particles and droplets),[6–11] active gels[12] and granular systems,[13] have unmasked universal physical principles that underlie non-equilibrium states found in both synthetic and living systems.[14–17] In particular, artificial self-propelled microswimmers that convert energy in their environment into states of matter far from equilibrium[6–11,18] have been shown to mimic key dynamical behaviors of motile organisms such as bacteria,[14,19] phytoplankton,[20] and epithelial cells.[21] For example, as oil droplets dissolve into aqueous micellar solutions,[22–24] they propel themselves *via* creation of interfacial tension gradients (Marangoni stresses) and exhibit behaviors such as chemotaxis.[6,9,17] Whereas past studies of self-propelled droplets have focused on single phase systems with spherical symmetry at rest, including single-phase droplets[6,10,18,25,26] and shells,[11] multiphase emulsion droplets with internal symmetry-broken morphologies (*e.g.*, Janus droplets[27–33]) with potential to program circulation internal to the droplets have not been explored.

When Janus droplets are dispersed into micellar solutions, they generally depart from being spherical[28,33] or break into two separate droplets.[31] These changes influence the motions of the droplets,[33] and thus mask efforts to understand how changes in internal domain structure impact dynamical behaviors. Furthermore, such shape changes prevent use of analytical models of microswimmers, such as the squirmer model,[34,35] as they assume spherical shapes. In this paper, we report an experimental approach that uses multi-phase oil droplets prepared from mixtures of hydrocarbon oils with nematic order and isotropic perfluorocarbon oils.[30] In contrast to other multiphase droplet systems, the oils droplets used in our study exhibit spherical shapes that are stable over a wide range of surfactant concentrations because the interfacial tension of the inner interface is two orders of magnitude lower than the outer two interfaces.[30] Here, we leverage this finding to explore the dynamics of self-propelled multiphase droplets that evolve in their internal morphology but maintain an overall spherical shape, and demonstrate how the rich dynamics displayed during morphogenesis can be mapped onto different squirmer types.

Living systems operate beyond equilibrium,[36] and morphogenesis of the structure of living systems is a strategy widely

[a] *Smith School of Chemical and Biomolecular Engineering, Cornell University, Ithaca, NY, USA. E-mail: nabbott@cornell.edu*
[b] *Institute for Molecular Engineering, University of Chicago, Chicago, IL, USA*
[c] *Argonne National Laboratory, Chicago, IL, USA*

† Electronic supplementary information (ESI) available. See DOI: 10.1039/d0sm01873b

‡ Authors contributed equally.

§ Current address: Department of Physics, The Hong Kong University of Science and Technology, Clear Water Bay, Kowloon, Hong Kong, China.

used by Nature to control emergent dynamics.[37,38] At macroscopic scales, the metamorphosis of a caterpillar into a butterfly transforms dynamics from crawling to flying.[37] Alternatively, at the microscopic scale, cellular differentiation of a stem cell into a cardiomyocyte generates a periodic contractile behavior that is responsible for the beating of the heart.[38] In contrast to the diverse examples of the impact of morphogenesis on dynamics encountered in active biological systems, the use of morphogenesis in synthetic soft matter systems as a strategy to program complex dynamics far from equilibrium has not been widely explored.[11] Here we show how multiphase oil droplets can be used as a model system to explore how morphogenesis of oil droplets impacts emergent dynamics driven by active processes.

The droplets used in our study undergo phase transitions from a single isotropic oil phase with low viscosity to biphasic Janus droplets with two domains with distinct viscosities and, ultimately, to a viscous nematic single-phase, as a consequence of the preferential solubilization (by a surrounding aqueous micellar solution) of specific components of the multicomponent oils. The evolution of the internal droplet morphology, as a function of time, generates a progression of five distinct droplet dynamical states that correlate strongly with droplet morphology. We find that the complex motions exhibited by the droplets can be described within the physical framework of the squirmer model for spherical microswimmers in Stokes flow.[34] Transitions between squirmer types were observed to accompany changes in droplet morphology, thus illustrating also how our experimental system provides a versatile platform for understanding and engineering microswimmers that display complex swimming patterns.[35,39,40]

Experiments

Materials

The nematogen, E7 (clearing temperature 60 °C), was purchased from HCCH (Jiangsu Hecheng Display Technology Co., Ltd). Hexafluorobenzene (99%, perfluorobenzene, FB), tetradecyltrimethylammonium bromide (≥99.0%, TTAB) and sodium dodecyl sulfate (≥99.0%, SDS) were purchased from Sigma-Aldrich (St. Louis, MO, USA). Fluorescent particles (FluoSpheres™ sulfate,1 μm diameter) were purchased from Life Technologies (Thermo Fisher Scientific). Fisher Finest Premium Grade glass slides was purchased from Fisher Scientific (Pittsburgh, PA). Purification of water (18.2 MΩ cm resistivity at 25 °C) was performed using a Milli-Q water system (Millipore, Bedford, MA, USA).

Preparation of samples without macroscopic surfactant concentration gradients

Optical cells were assembled from two glass slides separated from each other by ∼100 μm-thick spacers. 400 μl of E7 and 32 μl of FB were mixed by vortexing at 3000 rpm for 10 seconds, and 20 μl of the resulting oil mixture was dispersed into 1000 μl of aqueous 100 mM TTAB solution by gentle shaking of the mixture. We subsequently injected the mixture into optical cells and sealed the cells with silicone grease to avoid evaporation of water and unintended generation of surfactant concentration gradients. 100 mM TTAB solution was prepared using FB saturated water.

Preparation of samples with macroscopic surfactant concentration gradients

We performed a limited number of experiments in the presence of macroscopic surfactant concentration gradients (see Fig. 5 and associated text). To generate the samples with macroscopic concentration gradients, we left open one end of the optical cell to enable evaporation of water. When using 100 mM sodium dodecyl sulfate (SDS) or TTAB, we observed concentration gradients to form over a distance of ∼1 mm from the opening in the optical cell.

Droplet tracking

The temperature of each sample was controlled using a Linkam LTS350 hot stage with an accuracy of 0.1 °C. The trajectories of the oil droplets, along with the transitions from isotropic to biphasic to nematic phases, were recorded using a Canon EOS Rebel T6i camera at 30 fps under polarized light or fluorescent microscopy. Other videos were recorded using a Moticam 10+ camera. The motion of droplets ceased after ∼30 min with oil droplets still present. The droplet positions were extracted every 0.2 s using ImageJ and analyzed.

Measurement of droplet composition

50 μl of a FB–E7 mixture was dispersed into 10 ml of an aqueous TTAB (100 mM) solution and equilibrated at 85 °C overnight. After the oil droplets had sedimented and the overlying aqueous solution was removed, the oil phase was dissolved into hexane and analyzed using a JEOL gas chromatographic–mass spectrometer.

Results and discussion

Morphogenesis and dynamical motion of multiphase droplets

We used oil-in-water emulsions formed by mixing E7, a multicomponent nematic liquid crystal (LC; at room temperature) comprised of hydrogenated cyanobiphenyl and terphenyl species, with isotropic hexafluorobenzene (FB), and then mechanically dispersing the mixture as droplets in an aqueous phase of the surfactant TTAB (100 mM; TTAB has a critical micelle concentration (CMC) of 4 mM). We found that a FB–E7 mixture containing a 8 : 100 volume ratio, respectively, exhibited a single nematic phase below 32 °C; an isotropic phase above 40 °C; and nematic–isotropic phase coexistence between the two temperatures.[30] The experiments reported below were performed at 49 °C, at which temperature the oil mixture initially within the droplets was an isotropic phase (Fig. 1a). After dispersing the FB–E7 droplets in the aqueous surfactant solution, solubilization of select components of oil from the droplets over time caused the droplets to undergo a series of phase and morphological transitions (Fig. 1a–e). Specifically, we observed a nematic

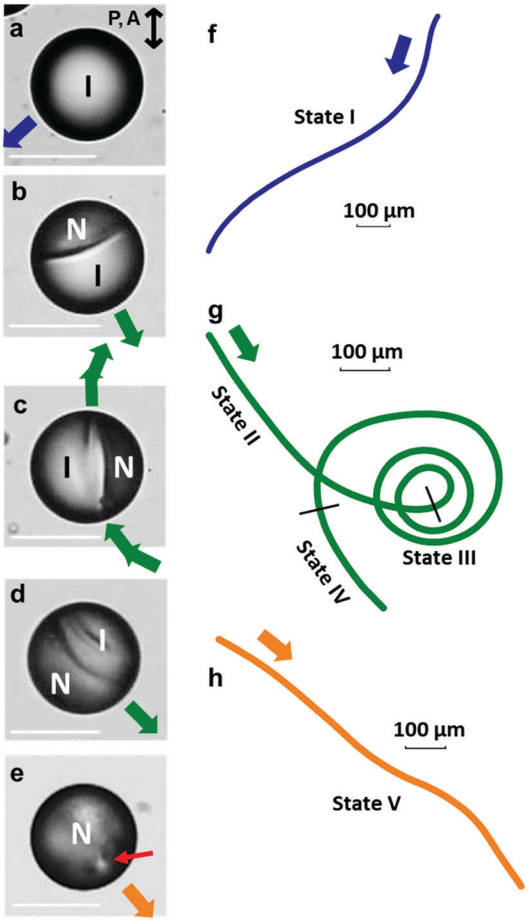

Fig. 1 Morphogenesis and dynamical motion of droplets. (a–e) Droplet morphologies under parallel polars and (f–h) corresponding trajectories observed during active droplet motion in the presence of 100 mM TTAB. I indicates an isotropic phase and N indicates a nematic phase. The blue, green and yellow arrows indicate directions of motion. The red arrow points to the defect of the nematic droplet. Scale bars for droplets are 50 μm.

domain to nucleate within isotropic phase droplets (Fig. 1b) and then grow (Fig. 1c and d) to eventually occupy the entire droplet volume (Fig. 1e). We confirmed that the above-described progression of phase states of droplets was due to preferential extraction of FB from the oil mixture within the droplets (Fig. S1, ESI†).[22,23]

The process of solubilization of oil from the droplets also generated interfacial tension gradients and interfacial flows that actively propelled the droplets through the surfactant solution.[10,17,24] To track the active motions of the droplets during the above-described changes in internal morphology, we confined the emulsion droplets within ~100 μm-thick optical cells filled with surfactant solution, sealed them with silicon grease to prevent evaporation of water, and then heated the system to 49 °C (isotropic phase droplets). The diameters of the droplets were between 30 and 85 μm, and typical speeds v ranged from 10 to 40 μm s^{-1}. By observing both droplet morphology and dynamics, we classified droplet motion into five dynamical states (State I to V, with increasing time).

During State I, the oil within the droplets comprised a single isotropic phase (Fig. 1a). We characterized trajectories over a duration of ~100 s (Fig. 1f) by evaluating the root mean squared displacement (RMSD) as a function of time interval t:[10,41,42] $\mathrm{RMSD} = \sqrt{\langle \Delta x^2(t) \rangle} = \sqrt{[\langle \boldsymbol{x}(t_0 + t) - \boldsymbol{x}(t_0) \rangle]^2}$, where $\boldsymbol{x}$ is the position vector of the droplet, t_0 samples all possible times on a trajectory (Fig. 2a), and the average is taken over all displacements occurring over time interval t (Fig. 2a). The RMSDs of the isotropic oil droplets were found to be proportional to time t over the duration of our observations (~100 s), indicating so-called ballistic motion.[10] The rotational diffusion coefficients of the droplets were calculated from the Stokes–Einstein relationship[43] as $D_r = k_B T/8\pi\eta r^3$, where k_B is the Boltzmann constant, T (323 K) is the temperature, η (10^{-3} Pa s) is viscosity of water, r (~10 μm) is the droplet size; we calculated D_r to be $\sim 2 \times 10^{-4}$ radians^2 s^{-1}, corresponding to a characteristic rotation period of 30 000 s that is much larger than the duration over which droplets were observed. Rotational diffusion, therefore, does not significantly influence droplet motion, consistent with the observation of ballistic trajectories.

As the solubilization process continued, we observed nematic domains to nucleate within the isotropic phase droplets (Fig. 1b). A nematic domain within an isotropic droplet (Janus droplet) did not perturb the ballistic trajectory for a period of ~ 30 s following the nucleation event (State II, Fig. 1g). In State II, the nematic domain localized at the trailing edge of the droplet with the inner interface (separating the nematic and isotropic domain) oriented perpendicular to the direction of motion. Whereas the equilibrium curvature of the inner interface of the nematic domain is concave,[30] we observed flows within the self-propelled droplets to deform the interface to a convex shape (Fig. 1b). Additional and more pronounced examples of flow-induced changes in internal morphology are described in Fig. 5.

As the volume of the nematic domain increased in size (Fig. 1c), the ballistic motion of the droplet became unstable and abruptly transformed to that of a spiral (State III, Fig. 1g and Video S1, ESI†), a dynamical state that persisted for ~200 s.

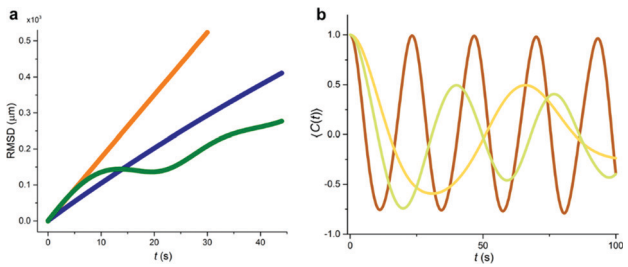

Fig. 2 Characterization of droplet trajectories. (a) RMSD of an isotropic (ballistic motion, blue), biphasic (spiraling motion, green) and nematic droplets (ballistic motion, yellow), respectively. The RMSDs were collected from independent experiments and thus document the behaviors of droplets with distinct sizes. (b) Autocorrelation of velocity of 3 biphasic droplets (56, 53 and 53 μm diameters) exhibiting spiraling trajectories at different temperatures (brown: 47 °C with average velocity of 18.4 μm s^{-1}; green: 49 °C with average velocity of 16.1 μm s^{-1}; yellow: 50 °C with average velocity of 11.5 μm s^{-1}).

Interestingly, accompanying this transition in dynamics, the inner interface rotated to align parallel to the direction of droplet motion (Video S2, ESI†), with the isotropic (nematic) domain consistently located on the outer (inner) side of the spiraling trajectory. The radius of the spiraling trajectory was not constant, but increased continuously over time, from 50 μm to 150 μm with increase in nematic domain size (State III, Fig. 1g). Typically, the Janus droplets executed 3–7 revolutions in State III. The dynamical behavior of the system was found to be achiral, with clockwise and counter-clockwise spirals observed with equal probability. We also observed the handedness of some droplet motions to switch during State III, with an accompanying reorganization of internal morphology (Fig. S2, ESI†). The spiraling motion was evident as an oscillatory feature in the calculated RMSD, following the functional form $a\sin(2\pi T + bt)$ (Fig. 2a), with scalars $a(t)$, b, time t and a rotation period T of 25 s.

The transition from dynamical State III to State IV was denoted by the resumption of ballistic motion (Fig. 1d and g, Video S1, ESI†), which persisted for ~30 s. In contrast to State II, however, the inner interface during State IV was oriented parallel to the direction of droplet motion (same as State III). State IV ended when the isotropic domain shrank to a topological defect that was then convected by internal flow within the droplet to the leading edge (Fig. S3, ESI†), as described elsewhere.[10,30] During dynamical State V (single nematic phase), the droplet exhibited a ballistic motion (RMSD $\propto t$, Fig. 2a). We note that past studies have reported that the type of trajectory exhibited by a single phase nematic droplet (*e.g.*, straight or curly) changes with droplet velocity, which in turn depends on both surfactant concentration and droplet size.[10,25] The relevant dimensionless parameter is the Ericksen number $\mathrm{Er} = v\eta r/K$, where v is the velocity of droplet, η is a characteristic viscosity of the LC, r is the droplet radius and K is a characteristic elastic constant of the nematic phase (one constant approximation). The Ericksen number characterizes the relative importance of viscous and elastic stresses; for small Ericksen numbers, the flow is not able to break the symmetry of the director field (including location of defect) that causes the curly motion of single phase droplets. The crossover from ballistic to curly motion is reported in ref. 25 to occur for Er of approximately 2. In our system $v \sim 10$ μm s^{-1}, $\eta \sim 10$ mPa s, $r \sim$ 15–50 μm, $K \sim 10$ pN, and thus Er ~ 0.15–0.5, consistent with the observation of a ballistic trajectory with a nematic phase droplet (single phase). From this result we also conclude that the origin of the spiraling motion observed during State III is the breaking of the droplet symmetry by the Janus morphology (see ESI†).[25]

To provide insight into the above behaviors, we evaluated the velocity autocorrelation function of spiraling State III trajectories as a function of time interval t:[41] $\langle C(t)\rangle = \left\langle \frac{\mathbf{v}(t_0+t)\cdot\mathbf{v}(t_0)}{|\mathbf{v}(t_0+t)|\cdot|\mathbf{v}(t_0)|}\right\rangle$, where $\mathbf{v}$ is the velocity vector of the droplet, t_0 samples all possible time values on a trajectory, and the average is taken over all pairs of velocities separated by time interval t. Fig. 2b shows $C(t)$ calculated from spiraling trajectories measured at three different temperatures (and thus with three different droplet compositions). The oscillating characteristic $\propto \cos(2\pi T)$ with period T varies from 25 s to 70 s[10] (droplets at the higher temperatures exhibiting the longer periods). The increase in rotational period T arises from a lower droplet velocity (see caption of Fig. 2b), which in turn occurs because the biphasic state at higher temperature arises at a lower FB concentration,[30] and thus is accompanied by a lower rate of solubilization (Fig. S4, ESI†). In addition, we calculated average curvatures κ of the spiraling trajectories as:[44] $\langle\kappa(t_0)\rangle = \left\langle \frac{1}{R(t_0)}\right\rangle$, where R refers to radii of trajectories as a function of time t_0. The average curvature of each trajectory is similar ~0.013–0.016 μm^{-1}, corresponding to trajectories with diameters of around 150 μm.

We also performed experiments to determine if temperature-induced changes in phase state and morphology of the droplets would induce transitions in dynamical behaviors similar to those triggered by changes in composition. By increasing temperature by 1 °C (to cause the size of the nematic domain to decrease), we triggered droplet motion to change from spiraling (State III) back to ballistic with an inner interface that was oriented perpendicular to the direction of motion (State II) (Video S3, ESI†). Furthermore, after a droplet had exhibited all five dynamical states, by raising the temperature such that the droplet reentered the single isotropic phase state (Fig. S5 ESI,† the oil mixture with a lower FB concentration has a higher clearing temperature[30]), we observed the droplets to progress again through a second set of dynamical states (due to isothermal solubilization). By increasing the temperature each time a droplet completed a life cycle (from 47–53 °C), we observed droplets to progress through dynamical States I to V a total of five times. Overall, these results confirm that the dynamical behaviors exhibited by the droplets are programmed by the internal morphologies of the droplets.

Physical processes influencing dynamical behaviors of droplets

To develop an understanding of the physical mechanisms that underlie the transitions between different droplet dynamical states, we dispersed fluorescent microparticles (1 μm diameter) into the aqueous surfactant phase to quantify advection near the surface of the self-propelled droplets.[11,45] We note that anisotropic fluid properties associated with the liquid crystalline phase are not the origin of the spiraling behavior or the switch between ballistic and spiraling behaviors observed in our experiments (as discussed above, nematic single-phase droplets exhibited ballistic motions in our experiments). In contrast, as detailed below, the principal consequence of the presence of the liquid crystalline phase is that of creating a viscous oil domain. The influence of the elasticity of the liquid crystal on droplet motion is discussed further below.

We first discuss the origin of the spiraling motion (State III) and the subsequent transition back to ballistic motion (State IV). Our measurements with tracer particles revealed that the aqueous phase flow field near a spiraling droplet was asymmetric (Fig. 3a and Video S4, ESI†). Tracer particles near the I domain (left, red arrow) and N domain (right, yellow arrows) moved from the leading to the trailing face of the droplet with a

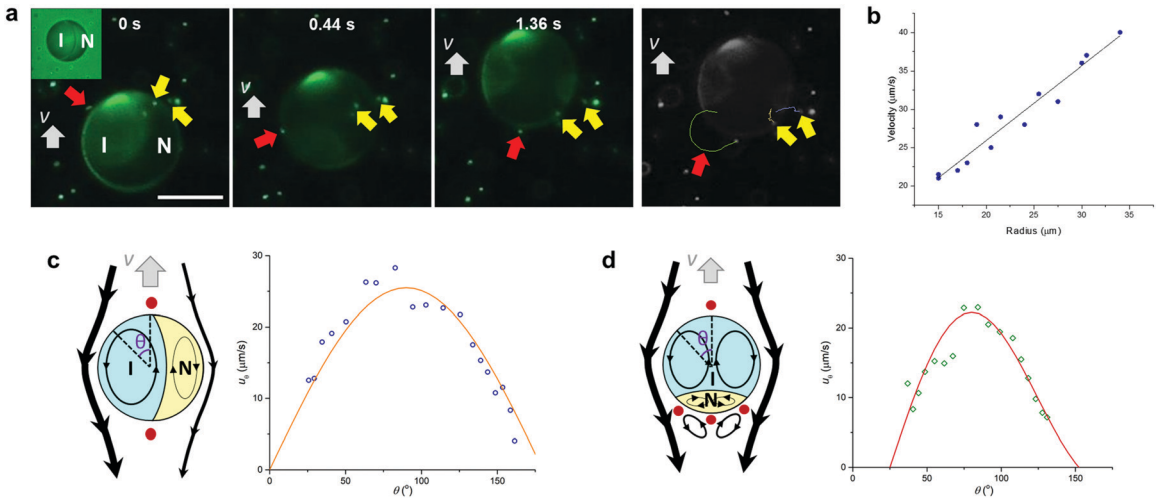

Fig. 3 Dynamics of droplets can be described by the squirmer model. (a) Time-lapse micrographs of tracer particles located near the surfaces of spiraling droplets. The large displacement of tracer particles near the isotropic domain is indicated by the red arrow, and the relatively smaller displacement of tracer particles near the nematic domain is shown by the yellow arrows. Scale bar, 50 μm. (b) Velocity of single-phase droplets formed from 4-pentyl-4′-cyanobiphenyl in 7.5% wt TTAB solution, plotted as a function of size (data from ref. 25). (c and d) Schematic illustrations and u_θ of tracer particles near surfaces of isotropic compartments of biphasic droplets in (c) State III (neutral-type squirmer) and (d) State II (puller-type). Black and gray arrows show direction of convective flow and direction of motion of droplets, respectively. Red dots ● denote stagnation points. Blue ○ and green ◇ dots are experimental data fit using eqn (4) with a phase shift (yellow and red, respectively).

trajectory that was dominated by fluid advection (not Brownian motion), but the displacement of tracer particles near the I interface of the droplet was greater than near the N interface. We formulated a scaling argument to predict the velocity of the interfaces of the I or N domains by assuming that the availability of free energy for propulsion is controlled by the rate of solubilization of the oil by the micellar solution, namely:

$$\alpha\pi r_{I/N}{}^2 c v_{I/N} f = F_{drag} v_{I/N} = \varphi\pi\eta_{I/N} r_{I/N} v_{I/N}{}^2 \quad (1)$$

where the left side describes the rate of generation of free energy by solubilization, with $r_{I/N}$ (μm) representing the size of I or N domain, c (mol m^{-3}) is the micelle concentration in the bulk aqueous solution, $v_{I/N}$ is the domain velocity, f (J mol^{-1}) is the effective free energy of solubilization and α is a scalar quantity. The center and right side terms of eqn (1) describe dissipation of energy due to drag, where F_{drag} is the drag force acting on the droplet, $\eta_{I/N}$ is effective viscosity of the I or N domain ($\eta_N \approx 3\eta_I$)[10,46] and φ is a scalar, respectively. Before using this model to describe Janus droplets, we tested the predictions of eqn (1) using single-phase droplets ($r_{I/N} \rightarrow r$, where r is the droplet radius), specifically that $v \propto \frac{cf}{\eta} r$. As $\frac{cf}{\eta}$ is determined by fluid properties, eqn (1) predicts that v is proportional to r for a given system. This prediction was tested against previously reported experimental data for oil droplets with radii smaller than 30 μm (for which interaction with walls is negligible)[25] and found to be in close agreement (Fig. 3b).

To apply eqn (1) to spiraling multi-phase droplets, we assumed $\frac{f_I}{f_N}$ to be of order 1 given the similarity in composition of the I phase (~ 4% FB) and N phases (~3% FB) at ~50 °C.[30] Although it is possible that f_I is slightly larger than f_N, since the I phase has a higher FB concentration and likely faster mass transfer (lower effective viscosity), our conclusion described below is not expected to change significantly during the motion analyzed (the compositions of the two phases in the biphasic region are constant, only the relative volumes of the two phases change over time). This leads to the prediction that the relative velocity of the N and I phases within the two compartments is given by:

$$\frac{v_I}{v_N} \propto \frac{r_I}{r_N}\frac{\eta_N}{\eta_I} \quad (2)$$

If I and N domains are similar in size ($r_I = r_N$), because $\eta_N > \eta_I$ ($\eta_N \approx 3\eta_I$),[10,46] eqn (2) predicts that $v_I > v_N$, thus generating a torque that leads to a spiraling motion with the I domain on the outside of the spiral. Furthermore, eqn (2) predicts that growth of the N domain will lead to a decrease in v_I/v_N, which in turn will result in a continuous increase in the radius of the spiraling trajectory as a function of time, as observed in experiments (Fig. 1g). When $r_I/r_N = 0.39$ (Fig. 4b, characterized by the ratio of perimeters of I *versus* N), the relative sizes of the N and I domains offset the relative viscosities, and thus $v_I \approx v_N$; droplet motion is predicted to be ballistic again. This condition corresponds to the onset of dynamical State IV, thus confirming that the spiraling behavior arises from compartmentalization of flow within the domains of the droplets. This contrasts to previous observations of helical motions of LC droplets,[10,25,26,47] for which the interplay of nematic elasticity and the convective flow breaks the symmetry of the ballistic motion.

Next, we discuss the origin of the transition from ballistic (State II) to spiraling motion (State III). Because the Janus droplets reported here are spherical, we describe the droplet motion using a so-called 3-dimensional (3D) squirmer model[34] for spherical microswimmers in low Reynolds number flow

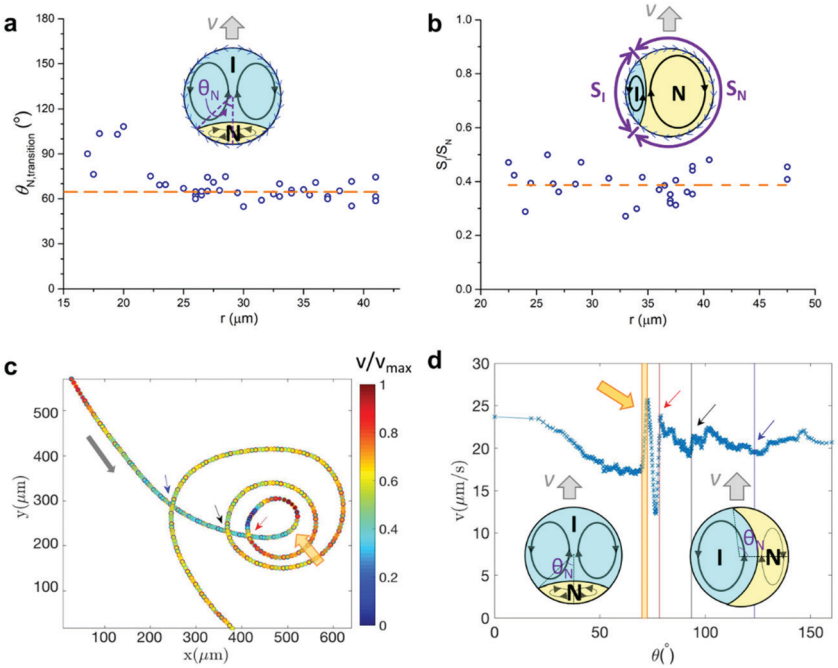

Fig. 4 Dynamical transitions of droplets. (a) Values of θ_N at the transition from ballistic (State II) to spiraling (State III) motion, plotted as a function of droplet radius. (b) Ratio of perimeters of I *versus* N at the transition from spiraling (State III) to ballistic (State IV), plotted as a function of droplet radius. Blue arrows in (a and b) show surface flow. (c) Trajectory of a Janus droplet with velocity shown by a color map with the transition from ballistic (State II) to spiraling (State III) motion marked by the yellow arrow. Red, black and blue arrows denote self-crossing of the droplet trajectory. The gray arrow shows the direction of motion. (d) Droplet velocity plotted as a function of θ, a descriptor of the N domain size. Arrows correspond to (c).

(Stokes flow). Three types of squirmers have been defined, namely pullers, pushers and neutral squirmers, each of which is characterized by a distinct flow field, as described below. In the laboratory frame, the flow fields are described by:[34]

$$u_r(\theta) = \frac{2}{3}B_1\cos\theta \quad (3)$$

$$u_\theta(\theta) = \frac{1}{3}B_1\sin\theta + \frac{1}{2}B_2\sin(2\theta) \quad (4)$$

$$\beta = \frac{B_2}{|B_1|} \quad (5)$$

where u_r and u_θ are the flow velocities perpendicular and tangential to the droplet interface, θ is the angle with respect to the motion direction, B_1 and B_2 are constants. The parameter β is used to categorize microswimmers as neutral squirmers ($\beta = 0$), pullers ($\beta > 0$) or pushers.[35]

Our analysis of tracer particle motion near the spiraling droplets (State III, Fig. 3c) revealed that the surface flow near the isotropic compartment exhibits two stagnation points, one at the leading edge and one at the trailing edge of the droplet. This droplet behavior was observed for a limited range of conditions, when the two phases within the droplets were comparable in volume and the inner interface between the two phases was aligned towards the direction of propagation of the droplet. Under these particular conditions, the fluid velocity profile near the droplet surface was measured in experiments to approximate that of a neutral squirmer (Fig. 3c, left). We fit the tracer velocity to the squirmer model (Fig. 3c), which revealed $B_2 \approx 0$ and $\beta \approx 0$, confirming that the experiments approximate neutral squirmer behavior. We note, however, that the biphasic droplet is not axisymmetric and thus β is not expected to be exactly zero (consistent with the presence of spiraling).[48] Our experiments also yielded an effective $B_1 \sim 76$ μm s^{-1} (yellow curve, Fig, 3c), which differs from the predicted value of $B_1 = \frac{3}{2}v \sim 40$ μm s^{-1}, where v is the droplet velocity, likely a consequence of asymmetric flow across the surface of the Janus droplets.

For droplets in State II, four stagnation points were observed (Fig. 3d), with the two additional stagnation points found near the three phase contact line towards the trailing edge. During State II, the flow field near the isotropic compartment changes as a function of the domain size. Fig. 3d shows one example where the inner interface is located at $\theta = 120°$, and the two additional stagnation points were found at $\theta = 130°$. Fitting of the experimental velocity data to the squirmer model reveals $B_2 \sim 42$ μm s$^{-1} > 0$ and $\beta = 0.54 > 0$, consistent with puller-type behavior; good agreement with the value of $\beta = 0.52$, estimated from the location of the stagnation points ($u_\theta(130°) = 0$) is also evident. A phase shift was observed for experimental values of u_θ (red curve, Fig. 3d), likely due to the effects of a density mismatch between tracer and aqueous fluid (inertia).

The evidence provided above leads us to conclude that the transition from the ballistic (State II) to the spiraling (State III) motion can be described as a switch from puller-type to neutral-type squirmer behavior. We quantified the morphology of the

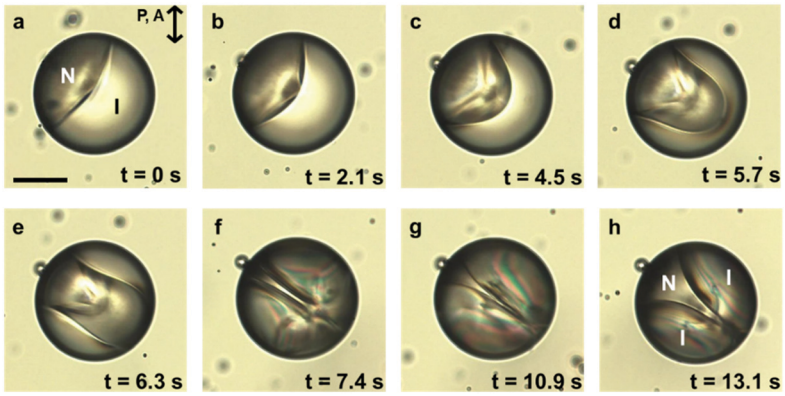

Fig. 5 Time-lapse micrographs showing the reorganization of the internal structure of a droplet with an initial biphasic (N–I) Janus morphology, with the I domain breaking into two lobes when moving towards the bottom right along an external surfactant concentration gradient. Scale bar, 50 μm.

two-compartment droplet at the transition between squirmer behaviors by the angle θ_N defining the relative size of nematic and isotropic compartments (Fig. 4a); the value of θ_N at the ballistic-to-spiraling transition was found to be about 65°. We also observed that smaller droplets transitioned from puller (State II) to neutral squirmer (State III) at larger values of θ_N. This size-dependence likely reflects a competition between viscous and elastic stresses within the LC droplet,[25] as characterized by the Ericksen number $v\eta r/K$ (elastic stresses dominate with decrease in r).

We generated a color map of the droplet velocity along its trajectory (Fig. 4c) as a function of θ_N (Fig. 4d). Interestingly, the droplet gained velocity, from 17 μm s^{-1} to 25 μm s^{-1}, during the transition from State II to State III, as denoted by the yellow arrow. The change in velocity is accompanied by a decrease in the number of vortices, from four to two, in the puller and neutral squirmer, respectively, and thus a decrease in viscous dissipation within the oil domains. In addition, in contrast to the neutral squirmer, the nematic domain within State II exhibits flow against droplet motion, likely contributing to the lower droplet velocity in State II. We also observed fluctuations in droplet velocities when droplets spiraled across their own trajectory (red, black and blue arrows in Fig. 4c and d), a phenomenon caused by negative autochemotaxis (see Fig. S6, ESI†).[47]

Morphogenesis and droplet behavior in the presence of external surfactant gredients

In the presence of external gradients in surfactant concentration, we found that droplet motion can dramatically reconfigure internal morphology to increase the number of internal domains. Fig. 5 shows droplets migrating along SDS gradients (Fig. 5 and Video S5, or TTAB gradients, Fig. S7, ESI†), moving to the bottom right corner where the SDS concentration was highest. The observation in Fig. 5 was recorded at 53 °C, with the droplet motion corresponding to State II (nematic domain trailing the motion (Fig. 5a)). With increase in speed of the droplet along the concentration gradient, we observed advection inside the droplet to deform the inner interface (Fig. 5b–g). Ultimately, the isotropic domain broke into two lobes (Fig. 5h).

Past studies have shown that the coupling of advection and solubilization can generate sustained interfacial tension gradients (Marangoni stresses) across droplet surfaces.[17] The rate of energy dissipation due to the surface flow[17] can be estimated as $\sim 2\pi r v \Delta\gamma$, where $r \sim 10^{-5}$ m is the radius of the droplet, $v \sim 10^{-5}$ m s^{-1} is the droplet velocity, and $\Delta\gamma$ is the change in interfacial tension across the aqueous interface of the droplet. We estimate that the energy stored in the inner interface increases by $\sim \pi r^2 \gamma$ over approximately Δt = 5 s, where γ is the interfacial tension of the inner interface, measured to be of order 10^{-5} N m^{-1}.[30] Because the work done over 5 s by the interfacial tension gradient acting on the droplet outer interface ($2\pi r v \Delta\gamma \Delta t$) must be larger than the energy stored in the extended inner interface ($\pi r^2 \gamma$), we conclude that $\Delta\gamma > 10^{-6}$ N m^{-1}. We note that this value is small compared to the absolute values of the interfacial tensions of the outer interfaces ($\sim 10^{-3}$ N m^{-1}) and thus consistent with our observation that the droplets are spherical during self-propelled motion (model spherical squirmers). Overall, this result emphasizes the complex interplay between morphology and dynamics that exists in this active, multiphase emulsion system.

Conclusions

We have used multiphase oil droplets to reveal how morphogenesis of domains internal to the droplets can impact emergent dynamics when driven by active processes. Our experimental approach embeds a number of advances in soft matter science, including the design of multiphase droplets with low internal interfacial tensions (that maintain spherical microswimmer geometry), and selective solubilization of components of the droplets by micellar extraction, leading to both morphogenesis and self-propulsion. We show that morphogenesis of the emulsion droplets and emergent changes in dynamics, including cycles of ballistic and spiraling behaviors, can be described within the physical framework of squirmer models for spherical microswimmers in Stokes flow. This framework has the potential to provide insight into experimental observations such as the number of vortices within the multi-compartment droplets, the reorientation of the inner interface,

and the increase in velocity of the droplets associated with the State II to State III transition. Overall, our results open new opportunities for future experimental studies of the behaviors and interactions of various types of squirmers. In the long-term, such studies offer the potential to guide the engineering of functional soft matter systems that exhibit the complexity of behaviors and functions found in living systems that undergo morphogenesis (*e.g.*, ability to change form in response to environment to modify dynamics).

Conflicts of interest

There are no conflicts to declare.

Acknowledgements

The authors acknowledge support from the Department of Energy, Basic Energy Sciences, Division of Materials Research, Biomaterials Program under Grant No. DE-SC0019762. The authors also thank Gaojin Li and Don Koch of Cornell University for insightful discussions.

Notes and references

1 L. Berthier and J. Kurchan, *Nat. Phys.*, 2013, **9**, 310–314.
2 B. X. Li, V. Borshch, R. L. Xiao, S. Paladugu, T. Turiv, S. V. Shiyanovskii and O. D. Lavrentovich, *Nat. Commun.*, 2018, **9**, 1–10.
3 A. U. Oza, L. Ristroph and M. J. Shelley, *Phys. Rev. X*, 2019, **9**, 041024.
4 H. R. O. Sohn and I. I. Smalyukh, *Proc. Natl. Acad. Sci. U. S. A.*, 2020, **117**, 6437–6445.
5 A. Izzet, P. G. Moerman, P. Gross, J. Groenewold, A. D. Hollingsworth, J. Bibette and J. Brujic, *Phys. Rev. X*, 2020, **10**, 021035.
6 T. Toyota, H. Tsuha, K. Yamada, K. Takakura, T. Ikegami and T. Sugawara, *Chem. Lett.*, 2006, **35**, 708–709.
7 J. R. Howse, R. A. L. Jones, A. J. Ryan, T. Gough, R. Vafabakhsh and R. Golestanian, *Phys. Rev. Lett.*, 2007, **99**, 048102.
8 F. Kümmel, B. ten Hagen, R. Wittkowski, I. Buttinoni, R. Eichhorn, G. Volpe, H. Löwen and C. Bechinger, *Phys. Rev. Lett.*, 2013, **110**, 198302.
9 Z. Izri, M. N. van der Linden, S. Michelin and O. Dauchot, *Phys. Rev. Lett.*, 2014, **113**, 248302.
10 C. Krüger, G. Klös, C. Bahr and C. C. Maass, *Phys. Rev. Lett.*, 2016, **117**, 048003.
11 B. V. Hokmabad, K. A. Baldwin, C. Krüger, C. Bahr and C. C. Maass, *Phys. Rev. Lett.*, 2019, **123**, 178003.
12 A. R. Bausch and K. Kroy, *Nat. Phys.*, 2006, **2**, 231–238.
13 N. Kumar, H. Soni, S. Ramaswamy and A. K. Sood, *Nat. Commun.*, 2014, **5**, 1–9.
14 J. P. Celli, B. S. Turner, N. H. Afdhal, S. Keates, I. Ghiran, C. P. Kelly, R. H. Ewoldt, G. H. McKinley, P. So, S. Erramilli and R. Bansil, *Proc. Natl. Acad. Sci. U. S. A.*, 2009, **106**, 14321–14326.
15 E. Lauga and T. R. Powers, *Rep. Prog. Phys.*, 2009, **72**, 096601.
16 V. Schaller, C. Weber, C. Semmrich, E. Frey and A. R. Bausch, *Nature*, 2010, **467**, 73–77.
17 S. Herminghaus, C. C. Maass, C. Krüger, S. Thutupalli, L. Goehring and C. Bahr, *Soft Matter*, 2014, **10**, 7008–7022.
18 F. Lancia, T. Yamamoto, A. Ryabchun, T. Yamaguchi, M. Sano and N. Katsonis, *Nat. Commun.*, 2019, **10**, 1–8.
19 E. Lauga, W. R. DiLuzio, G. M. Whitesides and H. A. Stone, *Biophys. J.*, 2006, **90**, 400–412.
20 J. S. Guasto, R. Rusconi and R. Stocker, *Annu. Rev. Fluid Mech.*, 2012, **44**, 373–400.
21 A. S. Chin, K. E. Worley, P. Ray, G. Kaur, J. Fan and L. Q. Wan, *Proc. Natl. Acad. Sci. U. S. A.*, 2018, **115**, 12188–12193.
22 P. D. Todorov, P. A. Kralchevsky, N. D. Denkov, G. Broze and A. Mehreteab, *J. Colloid Interface Sci.*, 2002, **245**, 371–382.
23 K. Peddireddy, P. Kumar, S. Thutupalli, S. Herminghaus and C. Bahr, *Langmuir*, 2012, **28**, 12426–12431.
24 C. C. Maass, C. Krüger, S. Herminghaus and C. Bahr, *Annu. Rev. Condens. Matter Phys.*, 2016, **7**, 171–193.
25 M. Suga, S. Suda, M. Ichikawa and Y. Kimura, *Phys. Rev. E*, 2018, **97**, 062703.
26 T. Yamamoto and M. Sano, *Soft Matter*, 2017, **13**, 3328–3333.
27 L. D. Zarzar, V. Sresht, E. M. Sletten, J. A. Kalow, D. Blankschtein and T. M. Swager, *Nature*, 2015, **518**, 520.
28 J. Jeong, A. Gross, W.-S. Wei, F. Tu, D. Lee, P. J. Collings and A. G. Yodh, *Soft Matter*, 2015, **11**, 6747–6754.
29 T. Nisisako, *Curr. Opin. Colloid Interface Sci.*, 2016, **25**, 1–12.
30 X. Wang, Y. Zhou, Y.-K. Kim, M. Tsuei, Y. Yang, J. J. de Pablo and N. L. Abbott, *Soft Matter*, 2019, **15**, 2580–2590.
31 N. Pannacci, H. Bruus, D. Bartolo, I. Etchart, T. Lockhart, Y. Hennequin, H. Willaime and P. Tabeling, *Phys. Rev. Lett.*, 2008, **101**, 164502.
32 X. Wang, Y. Zhou, V. Palacio-Betancur, Y.-K. Kim, L. Delalande, M. Tsuei, Y. Yang, J. J. de Pablo and N. L. Abbott, *Langmuir*, 2019, **35**, 16312–16323.
33 M. Li, M. Brinkmann, I. Pagonabarraga, R. Seemann and J.-B. Fleury, *Commun. Phys.*, 2018, **1**, 23.
34 J. R. Blake, *J. Fluid Mech.*, 1971, **46**, 199.
35 G.-J. Li and A. M. Ardekani, *Phys. Rev. E*, 2014, **90**, 013010.
36 L. Berg, E. Solomon and D. W. Martin, *Biology, Boorks/Cole*, Cengage Learning, USA, 2011.
37 J. L. Capinera, *Encyclopedia of entomology*, Springer Science & Business Media, 2008.
38 N. J. Severs, *BioEssays*, 2000, **22**, 188–199.
39 S. Van Teeffelen and H. Löwen, *Phys. Rev. E*, 2008, **78**, 020101.
40 R. Wittkowski and H. Löwen, *Phys. Rev. E*, 2012, **85**, 021406.
41 N. Tarantino, J.-Y. Tinevez, E. F. Crowell, B. Boisson, R. Henriques, M. Mhlanga, F. Agou, A. Israël and E. Laplantine, *J. Cell Biol.*, 2014, **204**, 231–245.
42 S. Burov, S. M. Ali Tabei, T. Huynh, M. P. Murrell, L. H. Philipson, S. A. Rice, M. L. Gardel, N. F. Scherer and A. R. Dinner, *Proc. Natl. Acad. Sci. U. S. A.*, 2013, **110**, 19689–19694.
43 K. L. Ngai, Relaxation and diffusion in complex systems, 2011.

44 A. Mjaavatten, Curvature of a 2D or 3D curve, https://www.mathworks.com/matlabcentral/fileexchange/69452-curvature-of-a-2d-or-3d-curve.
45 R. Seemann, J.-B. Fleury and C. C. Maass, *Eur. Phys. J.: Spec. Top.*, 2016, **225**, 2227–2240.
46 A. G. Chmielewski, *Mol. Cryst. Liq. Cryst.*, 1986, **132**, 339–352.
47 C. Jin, C. Krüger and C. C. Maass, *Proc. Natl. Acad. Sci. U. S. A.*, 2017, **114**, 5089–5094.
48 O. S. Pak and E. Lauga, *J. Eng. Math.*, 2014, **88**, 1–28.